



Effect of intense wind shear across the inversion on stratocumulus clouds

Shouping Wang,¹ Jean-Christophe Golaz,² and Qing Wang³

Received 17 March 2008; revised 12 May 2008; accepted 9 July 2008; published 13 August 2008.

[1] A large-eddy simulation model is used to examine the impact of the intense cross-inversion wind shear on the stratocumulus cloud structure. The wind shear enhanced entrainment mixing effectively reduces the cloud water and thickens the inversion layer. It leads to a reduction of the turbulence kinetic energy (TKE) production in the cloud layer due to the weakened cloud-top radiative cooling and the formation of a turbulent and cloud free sublayer within the inversion. The thickness of the sublayer increases with the enhanced wind shear intensity. Under the condition of a weaker inversion, the enhanced shear mixing within the inversion layer even lowers the cloud-top height and reduces the entrainment velocity. Finally, increasing wind shear or reducing inversion strength tends to create an inversion layer with a constant bulk Richardson number (~ 0.3), suggesting that an equilibrium value of the Richardson number is reached. **Citation:** Wang, S., J.-C. Golaz, and Q. Wang (2008), Effect of intense wind shear across the inversion on stratocumulus clouds, *Geophys. Res. Lett.*, 35, L15814, doi:10.1029/2008GL033865.

1. Introduction

[2] Turbulence dynamics of stratocumulus clouds has been investigated intensively since Lilly [1968] first developed the mixed-layer cloud model in which turbulence is maintained by the cloud-top longwave radiative cooling. Most of the investigations have been focused on the entrainment processes driven by the buoyancy forcing. Another source for the turbulence, which has drawn less attention in the past, is wind shear across the cloud-top inversion. Analyses of early field experiment data have revealed that the strong wind shear may dominate TKE production in the cloud-topped boundary layer (CTBL) [Brost *et al.*, 1982]. The turbulence mixing driven by the wind shear may lead to local dissipation of clouds [de Roode and Wang, 2007]. Moeng *et al.* [2005] analyzed their large-eddy simulation (LES) results and found that a cloud free and turbulence layer of several tens of meters is always present in the inversion due to local wind shear events. Both early and more recent observations have shown that the cloud top is indeed not the limit of the turbulence mixing [e.g., James, 1959; Lenschow *et al.*, 2000]. These studies clearly demonstrate the importance of the wind shear in the stratocumulus dynamics; they also raise the question: what is the funda-

mental difference between the strongly sheared and the shear-free stratocumulus convection?

[3] A low-level jet near the top of the CTBL is frequently observed off the California central coast during summer due to the topography and land-sea contrast [Strom *et al.*, 2001; Rahn and Parish, 2007]. Figures 1a–1c show soundings taken in an aircraft flight in the field experiment of Development and Evolution of Coastal Stratocumulus [Kalogiros and Wang, 2002]. The wind speed reaches maximum 18 ms^{-1} just below the base of the inversion; decreases by 8 ms^{-1} across the sharp inversion; and then reduces further but more gradually to 7 m s^{-1} at about 730 m. Observations like this provide an opportunity to explore the impact of the intense wind shear on the cloud and turbulence structure. In this study, a large-eddy-simulation (LES) model is used to investigate specific roles of the cross-inversion wind shear in the turbulence-cloud-radiation interaction; and highlight some fundamental differences in the cloud structure with and without the shear.

2. Simulation Setup

[4] An LES model was recently developed based on the Naval Research Laboratory Coupled Ocean/Atmosphere Mesoscale Prediction System (COAMPS[®]) [Golaz *et al.*, 2005]. The latest improvement of the model is the implementation of the four stream Fu-Liou radiation parameterization [Fu and Liou, 1992; Liu *et al.*, 2008]. Two sets of simulations are performed in this work; the first uses the observed inversion condition as shown in Figures 1a and 1b, the second uses weaker inversion strength. Each of the sets includes simulations with different wind shear conditions from the shear free to high intensity (see Table 1). Note that for the shear free case of each set, surface fluxes are specified based on the averaged values obtained from other two cases. Realizing that the resolution used in the simulations is not fine enough to resolve the turbulent motion in the inversion, we particularly perform a high-resolution simulation (case SSH in Table 1) for comparison purpose.

[5] To maintain the cross-inversion wind shear in the simulations, a mesoscale forcing is needed to represent both the mesoscale baroclinic geostrophic winds and the horizontal advection in the momentum equations. Due to the lack of mesoscale meteorological data, we simply use observed winds as geostrophic winds (Figure 1c) and specify a boundary-layer height dependent forcing profile; the sum of these two forcing result in the desired wind profiles (Figure 1d). This idealized approach is justified as long as the simulated wind profile is close to the observation. We also specify a mesoscale divergence (10^{-5} s^{-1}), which results in a boundary layer height consistent with the observation. The observed $\bar{\theta}_i$ and \bar{q}_i are used for the initial

¹Naval Research Laboratory, Monterey, California, USA.

²UCAR VSP, GFDL, NOAA, Princeton, New Jersey, USA.

³Naval Postgraduate School, Monterey, California, USA.

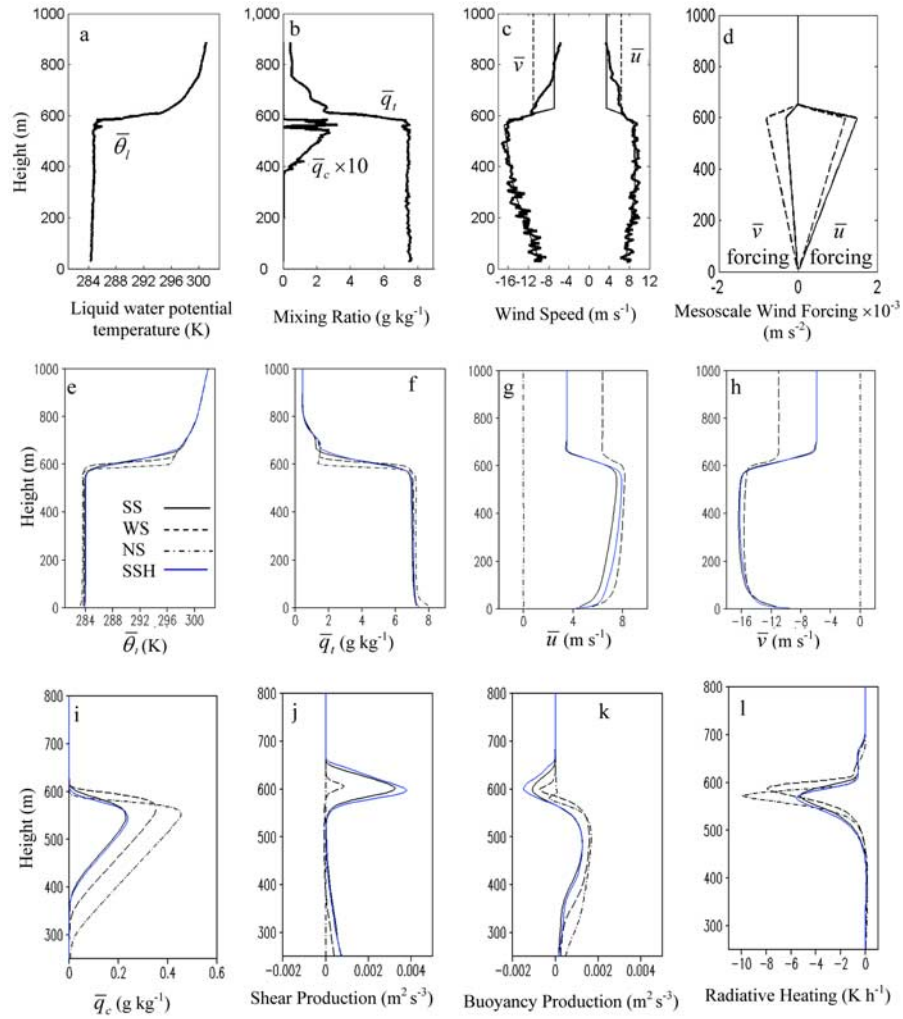


Figure 1. (a–c) The aircraft observations and (d–k) COAMPS-LES forcing and simulated mean profiles and TKE generation mechanisms. (a) Observed liquid water potential temperature $\bar{\theta}_l$. (b) Total water mixing ratio \bar{q}_t and liquid water mixing ratio \bar{q}_c . (c) the wind component toward the east u , the wind component toward the north v , and smooth thin lines denote the “target” wind profiles used for the nudging procedure and geostrophic winds (solid for the SS case and dashed for the WS case). (d) Additional mesoscale wind forcing used in the simulations with the solid for SS and dashed for WS. Simulated (e) $\bar{\theta}_l$, (f) \bar{q}_t , (g) \bar{u} , (h) \bar{v} , and (i) \bar{q}_c . (j) Shear production. (k) Buoyant production. (l) Longwave radiative heating rate. The observations were taken on 8 July 1999 near the location $(-122.4, 36.68)$.

profiles in all the simulations. To avoid an initial significant decrease of q_c due to the shear, a nudging procedure with a time scale 30 min is applied to force the wind toward the “target” profiles (see Figure 1c). The nudging is then terminated after the first hour. The wind is initialized with a constant value equal to the “target” winds above the inversion. All the statistics presented are based on the LES explicitly resolved flows and are calculated between 6 and 8 hours with a sample interval of 30s unless specified otherwise.

3. Results

[6] We discuss results from the first set of simulations (Strong Inversion) in 3.1 and 3.2; then the second (Weak Inversion) in 3.3.

3.1. Mean Profiles and TKE-Production

[7] As shown in Figures 1e and 1f, a stronger cross-inversion wind shear tends to result in a warmer, drier and slightly deeper boundary layer, indicating that the stronger shear produces more intense entrainment. Cloud water \bar{q}_c is shown to decrease with the increasing wind shear in Figure 1i. The cloud-top heights (defined by the level at which \bar{q}_c or cloud fraction vanishes) from the three cases remain similar despite the significant difference in \bar{q}_c . The wind shear is very different in SS and WS as designed. The simulated \bar{v} is apparently more uniform than the observation below 300 m, suggesting that the mesoscale forcing at those levels may need to be enhanced to balance the momentum mixing. There is a very sharp inversion in the shear free case (NS) due to the strong radiative cooling and a lack of turbulence generation in the inversion zone. The SS case results in a significantly thicker inversion layer due to the

Table 1. Simulation Setup and Some Results^a

Case	Wind Shear Intensity	Surface Condition	Initial Inversion Strength	Resolution	Results: Fluxes (Wm ⁻²)	Results: w_e (cm s ⁻¹)
<i>Strong Inversion</i>						
SS	Strong	Interactive SST = 284.5K	12K	$\Delta z = 5 - 20\text{m}$ $\Delta x = \Delta y = 30\text{m}$	SH = -10 LH = 50	0.71
WS	Weak	—	—	—	SH = -8 LH = 53	0.66
NS	No mean wind	SH = -9 W/m ² LH = 51 W/m ²	—	—	—	0.59
SSH	—	—	—	$\Delta x = \Delta y = 10\text{ m}$ $\Delta z = 5\text{ m}$	SH = -11 LH = 49	0.68
<i>Weak Inversion</i>						
SSI	—	—	10K	—	SH = -10 LH = 52	0.82
WSI	Weak	—	10K	—	SH = -12 LH = 57	0.88
NSI	No mean wind	SH = -11 Wm ⁻² LH = 55 Wm ⁻²	10K	—	—	1.2

^aA dash indicates the same as in the SS case; SH, sensible heat flux; LH, latent heat flux; time averaged w_e is calculated based on the inversion-top height (\bar{z}_i^θ) as defined in Table 2.

wind shear generated turbulence. The WS-case wind shear also has the same effect, although to a less degree.

[8] The largest TKE shear production in the inversion occurs at the level of the largest TKE buoyancy consumption, suggesting that the entrainment is primarily produced locally by the wind shear as shown in Figures 1j and 1k. The maximum value of the buoyancy consumption increases by about 4 times from the NS to the SS case, even though the positive TKE buoyancy production of the former is the largest.

[9] The positive TKE buoyancy production in the cloud layer is decreased in the WS and SS cases compared to the NS case mainly because the decreased liquid water leads to a substantial reduction in the cloud-top radiative cooling rate (Figures 1k and 1l). This buoyancy production decrease is also caused by the intense entrainment manifested with the large TKE consumption in two shear cases. Since the cloud-layer buoyancy is the main driving force for the large eddy convective circulation, the wind shear may actually weaken the convection. This process represents a major difference between the sheared convection with and without clouds. For the former, the shear may considerably weaken the strength of the TKE buoyancy production through the cloud-longwave radiation interaction; for the latter, it can only moderately affect the surface buoyancy flux through the entrainment of warmer air. It is also noticed that the results of the high-resolution simulation (SSH) are very close to those of the coarse-resolution (SS) as shown in Figures 1e–1l.

3.2. Inversion Layer Characteristics

[10] Since the turbulence variance of a scalar is proportionally linked to the mean vertical gradient and the turbulence intensity, $\overline{\theta_1^2}$ profile provides a good measure of the inversion thickness. The variance $\overline{\theta_1^2}$ becomes more broadly distributed in the inversion layer from the NS to the SS case as shown in Figure 2a. For the NS case, both $\overline{\theta_1^2}$ and the cloud fraction appear to diminish at about the same height; while for the SS case, $\overline{\theta_1^2}$ clearly extends to higher levels than the cloud fraction.

[11] To quantitatively compare the cloud-top, inversion-top and inversion-base levels, we further define these heights by specifying cut-off values for various relevant mean or turbulence variables in Table 2; this is done by carefully comparing the vertical profiles of the mean and turbulence variables. The time series of the various heights based on one-minute samples are presented in Figures 2e–2g. For the NS case, \bar{z}_i^{ke} is about at the same level as \bar{z}_i^θ ; both of them approximately follow the running mean of the cloud top height (z_i^c). For both the WS and the SS cases, the inversion layer top heights, \bar{z}_i^{ke} and \bar{z}_i^θ , are higher than the cloud tops, indicating the presence of a turbulent and clear sublayer within the inversion. The thickness of this layer is about 15–20 m for WS. For the SS case, it is about 30–35 m when \bar{z}_i^θ is used; the thickness increases to 70 m when \bar{z}_i^{ke} is used in the estimation. Although TKE may be well above zero above \bar{z}_i^θ in the SS case, the mean $\bar{\theta}_1$ profile shows little effect of turbulence at heights between \bar{z}_i^θ (662 m) and \bar{z}_i^{ke} (701 m) as indicated by the results in Table 2 and Figures 2a–2d. Therefore, \bar{z}_i^θ appears to represent the inversion-top height more realistically in this case. The domain average cloud top heights (\bar{z}_i^m) are actually very close to the inversion base heights (\bar{z}_i^b). The inversion layer thickness ($\bar{z}_i^\theta - \bar{z}_i^b$) increases from only 30 m in the NS to 45 m in the WS case; it further increases to 95m in the SS case. Although these quantitative results depend on the specific cut-off values, the overall qualitative behavior of these heights is clear. That is, the shear free CTBL is the closest to the view of the mixed-layer theory for which the sharp inversion defines both the cloud top and the boundary layer top heights; the separation of the two levels in these cases is primarily driven by the turbulence mixing generated by the mean wind shear; and its thickness increases with the mean wind shear. Our result is different from that of Moeng *et al.* [2005], which shows that the clear and turbulent sublayer is caused by the local shear events, not by the mean shear.

3.3. Impact of Inversion Strength

[12] To study the effect of the inversion strength, we perform three additional simulations (NSI, WSI, and SSI),

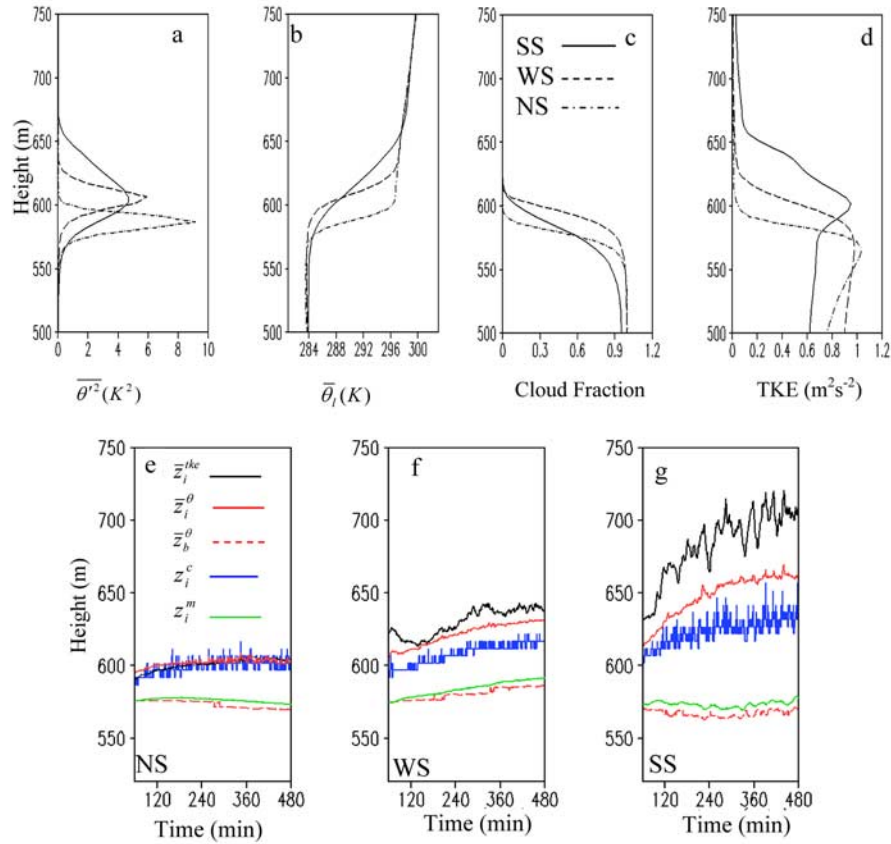


Figure 2. Inversion layer characteristics. Vertical profiles of (a) $\overline{\theta^2}$, (b) $\overline{\theta}_i$, (c) cloud fraction, and (d) TKE; line types are denoted in Figure 2c. Time series of various height levels of (e) NS, (f) WS, and (g) SS; line types are denoted in Figure 2e.

whose conditions are the same as those of the previous cases (NS, WS and SS) except that $\overline{\theta}_i$ above the initial inversion layer is reduced by 2K as described in Table 1.

[13] A major difference between this set of simulations (i.e., NSI, WSI and SSI) and the one with the strong inversion (i.e., NS, WS and SS) is the apparent decrease of the cloud-top height with the increasing wind shear in the former (Figure 3a versus Figure 1i). This is because the enhanced wind shear mixing due to the weaker inversion significantly reduces the cloud water. The maximum \overline{q}_c decreases by 0.25 gkg^{-1} from NSI to SSI compared to 0.21 gkg^{-1} from NS to SS; it decreases by 0.21 from NSI to WSI compared to 0.12 gkg^{-1} from NS to WS. This significant decrease in \overline{q}_c considerably weakens the cloud-

top radiative cooling, leading to a reduction in the positive buoyancy flux (not shown). Furthermore, the enhanced shear results in a lift of the cloud base in the strong inversion cases (Figure 1i); but it changes the cloud base level much less in the weak inversion cases (Figure 3a). It suggests that the entrained dry air tend to remain in the inversion layer in the weak inversion cases; while they are more likely brought into the mixed layer by the convective circulation in the strong inversion cases.

[14] The time-averaged entrainment velocity (the last column in Table 1), defined by the temporal derivative of \overline{z}_i^θ minus the large-scale vertical motion at \overline{z}_i^θ , increases with the intensified shear for the strong inversion cases; while it decreases with the shear in the weak inversion cases. This

Table 2. Definition of Various Height Levels and Time-Averaged Results

Variables	Definition	Cut-Off Value	Results Based on Profiles in Figure 2
\overline{z}_i^{tke}	CTBL top defined by horizontal-domain averaged TKE	$0.05 \text{ m}^2\text{s}^{-2}$ from top	NS: 601 m WS: 628 m SS: 701 m
\overline{z}_i^θ	CTBL top defined by $\overline{\theta^2}$	0.1 K^2 from top	NS: 605 m WS: 630 m SS: 662 m
\overline{z}_b^θ	Inversion layer base defined by $\overline{\theta_i^2}$	0.5 K^2 from surface	NS: 568 m WS: 583 m SS: 567 m
\overline{z}_i^c	Cloud top defined by the highest level where a grid is saturated in the domain.	N/A	N/A
\overline{z}_i^m	Domain averaged cloud-top height	N/A	N/A

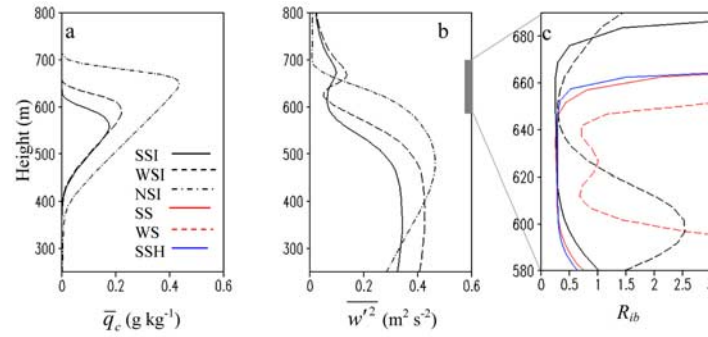


Figure 3. Impact of inversion strength: (a) \bar{q}_c , (b) $\overline{w'^2}$, and (c) bulk Richardson number. Note that the vertical extent of Figure 3c is different from that of Figure 3a or Figure 3b; it only represents the shaded region in Figure 3b.

demonstrates the complex role of the wind shear: on the one hand, it increases the shear mixing; on the other hand, if the mixing in the inversion is strong enough to sufficiently reduce the cloud water, the overall entrainment intensity may be weakened because the radiative cooling can be significantly reduced.

[15] We define following bulk Richardson number:

$$R_{ib} = \frac{g}{\theta_{vl}} \frac{\Delta \bar{\theta}_{vl} \Delta z}{[(\Delta \bar{u})^2 + (\Delta \bar{v})^2]},$$

where Δ is the difference in the neighboring grid points in the vertical and θ_{vl} the virtual liquid water potential temperature. Figure 3c shows R_{ib} profiles within the inversion from the five cases of WS, SS, WSI, SSI and SSH. The main points shown by Figure 3c are threefold. First, the Richardson number remains almost constant (~ 0.3) within the inversion for the SS and the SSI cases even though their inversion strength is different. Second, it decreases with either the weakened inversion (WS to WSI) or the enhanced wind shear (WS to SS; WSI to SSI). Third, the decreased Richardson number of the WSI case approaches to and is greater than the value (0.3). The results appear to suggest that a dynamic process is taking place to adjust the Richardson number to its equilibrium value (~ 0.3 in this case) within the inversion, as discussed by Turner [1973]. That is, a Richardson number smaller than the equilibrium value would strengthen mixing; and the inversion would thicken so that the Richardson number would increase and adjust to its equilibrium value. Conzemius and Fedorovich [2006] attributed a similar phenomenon in the simulated sheared dry convective boundary layer (CBL) to the balance between TKE-production and consumption. The high-resolution simulation (SSH) produces a Richardson number that is very close to the coarse-resolution (SS) as shown in Figure 3c, a further indication that high-resolution simulations should not qualitatively change the conclusions obtained based on the coarse-resolution simulations.

4. Summary

[16] Wind shear always occurs across the inversion; its impact varies depending on its intensity and other large-scale conditions as shown in this observation-based COAMPS-LES study. The intense wind shear enhances the entrainment mixing within the inversion to significantly reduce cloud

liquid water mixing ratio and thickens the inversion layer, leading to the formation of a turbulent and cloud free sublayer. The reduction in the liquid water leads to a decreased cloud-top longwave radiative cooling, which weakens the TKE buoyancy production in the cloud layer. Under the condition of a weaker inversion, the enhanced entrainment mixing due to the stronger shear actually lowers the cloud-top height because the cloud water is significantly reduced. Consequently, an enhanced wind shear may result in a reduced entrainment velocity. This is in contrast to the thermally driven and shear free CTBL in which an enhanced thermal forcing (e.g., increasing SST) tends to increase both the cloud top and the entrainment velocity except probably for the conditions of the cloud-top entrainment instability and cloud-layer decoupling [Yamaguchi and Randall, 2008; Bretherton and Wyant, 1997]. The result is also different from a dry sheared CBL where a stronger wind shear across the inversion would certainly enhance the entrainment since the surface buoyancy would not be significantly reduced by the shear. Finally, with increasing wind shear or reducing inversion strength, the inversion layer approaches to an equilibrium condition manifested by a constant, self-adjusting and equilibrium Richardson number (~ 0.3).

[17] **Acknowledgments.** We thank Ming Liu for implementing the new radiation package in COAMPS-LES, Qingfang Jiang for many useful discussions, and James Doyle for comments on an early version of the paper. We also greatly appreciate two reviewers' constructive comments, which result in improvement in the presentation. S. Wang acknowledges the support from the Office of Naval Research (ONR) under program element (PE) 0602435N. J.-C. Golaz was supported by the Visiting Scientist Program at the NOAA Geophysical Fluid Dynamics Laboratory, administered by the University Corporation for Atmospheric Research. Qing Wang acknowledges the ONR support under N0001407WR20229. COAMPS[®] is a registered trade mark of the Naval Research Laboratory.

References

- Bretherton, S. C., and M. C. Wyant (1977), Moisture transport, lower-tropospheric stability, and decoupling of cloud-topped boundary layers, *J. Atmos. Sci.*, *54*, 148–167.
- Brost, R. A., J. C. Wyngaard, and D. H. Lenschow (1982), Marine stratocumulus layers. Part II: Turbulence budgets, *J. Atmos. Sci.*, *39*, 818–836.
- Conzemius, R. J., and E. Fedorovich (2006), Dynamics of sheared convective boundary layer entrainment. Part I: Methodological background and large-eddy simulations, *J. Atmos. Sci.*, *63*, 1151–1178.
- de Rooze, R. S., and Q. Wang (2007), Do stratocumulus clouds detrain? FIRE I data revisited, *Boundary Layer Meteorol.*, *122*, 479–491.
- Fu, Q., and K.-N. Liou (1992), On the correlated k-distribution method for radiative transfer in nonhomogeneous atmospheres, *J. Atmos. Sci.*, *49*, 2139–2156.
- Golaz, J.-C., S. Wang, J. D. Doyle, and J. D. Schmidt (2005), COAMPSTM LES: Model evaluation and analysis of second and third moment vertical velocity budgets, *Boundary Layer Meteorol.*, *116*, 487–517.

- James, D. G. (1959), Observations from aircraft of temperature and humidities near stratocumulus clouds, *Q. J. R. Meteorol. Soc.*, *85*, 120–130.
- Kalogiros, J. A., and Q. Wang (2002), Calibration of a radome-differential GPS system on a Twin Otter research aircraft for turbulence measurements, *J. Atmos. Oceanic Technol.*, *19*, 159–171.
- Lenschow, D. H., M. Zhou, Z. Zeng, L. Chen, and X. Xu (2000), Measurements of fine-scale structure at the top of marine stratocumulus, *Boundary Layer Meteorol.*, *97*, 331–357.
- Lilly, D. K. (1968), Models of cloud-topped mixed layers under a strong inversion, *Q. J. R. Meteorol. Soc.*, *94*, 292–308.
- Liu, M., J. E. Nachamkin, and D. L. Westphal (2008), On the improvement of COAMPS weather forecasts by using an advanced radiative transfer model, *Weather Forecasting*, in press.
- Moeng, C.-H., B. Stevens, and P. P. Sullivan (2005), Where is the interface of stratocumulus-topped PBL?, *J. Atmos. Sci.*, *62*, 2626–2631.
- Rahn, D. A., and T. R. Parish (2007), Diagnosis of the forcing and structure of the coastal jet near Cape Mendocino using in situ observations and numerical simulations, *J. Appl. Meteorol.*, *46*, 1455–1468.
- Strom, L., M. Tjernstrom, and D. P. Rogers (2001), Observed dynamics of coastal flow at Cape Mendocino during coastal wave 1996, *J. Atmos. Sci.*, *58*, 953–977.
- Turner, J. S. (1973), *Buoyancy Effects in Fluids*, 368 pp., Cambridge Univ. Press, Cambridge, U. K.
- Yamaguchi, T., and D. A. Randall (2008), Large-eddy simulation of evaporatively driven entrainment in cloud-topped mixed layers, *J. Atmos. Sci.*, *65*, 1482–1504.

J.-C. Golaz, UCAR VSP, GFDL, NOAA, Princeton University, Forrestal Campus, US Route 1, PO Box 308, Princeton, NJ 08542, USA.

Q. Wang, Naval Postgraduate School, Monterey, CA 93943, USA.

S. Wang, Naval Research Laboratory, 7 Grace Hopper, MS2, Monterey, CA 93943, USA. (wang@nrlmry.navy.mil)